MODELLING AND SIMULATION OF LASER INDUCED PERIODIC SURFACE STRUCTURING

A THESIS SUBMITTED TO
THE GRADUATE SCHOOL OF NATURAL AND APPLIED SCIENCES
OF
MIDDLE EAST TECHNICAL UNIVERSITY

BY

MAHMUT SİNAN YAYLA

IN PARTIAL FULFILLMENT OF THE REQUIREMENTS
FOR
THE DEGREE OF MASTER OF SCIENCE
IN
PHYSICS

JANUARY 2023

Approval of the thesis:

MODELLING AND SIMULATION OF LASER INDUCED PERIODIC SURFACE STRUCTURING

submitted by **MAHMUT SİNAN YAYLA** in partial fulfillment of the requirements for the degree of **Master of Science in Physics, Middle East Technical University** by,

Prof. Dr. Halil Kalıpçılar
Dean, Graduate School of **Natural and Applied Sciences** _____

Prof. Dr. Seçkin Kürkçüoğlu
Head of the Department, **Physics** _____

Assist. Prof. Dr. Ihor Pavlov
Supervisor, **Physics, METU** _____

Examining Committee Members:

Prof. Dr. Halil Berberoğlu
Physics, Ankara Hacı Bayram Veli University _____

Assist. Prof. Dr. Ihor Pavlov
Physics, METU _____

Prof. Dr. Alpan Bek
Physics, METU _____

Date: 24.01.2023

I hereby declare that all information in this document has been obtained and presented in accordance with academic rules and ethical conduct. I also declare that, as required by these rules and conduct, I have fully cited and referenced all material and results that are not original to this work.

Name Last name: Mahmut Sinan Yayla

Signature:

ABSTRACT

MODELLING AND SIMULATION OF LASER INDUCED PERIODIC SURFACE STRUCTURING

Yayla, Mahmut Sinan
Master of Science, Physics
Supervisor: Assist. Prof. Dr. Ihor Pavlov

January 2023, 46 pages

In recent years, the interest in laser-induced periodic surface structuring (LIPSS) is increased due to its flexibility and cost efficiency. It is a promising alternative to the conventional ways of surface micro and nano structuring. Although, there are generally accepted and supported theoretical studies in the field, the phenomenon lacks a complete model. This thesis study presensts a theoretical model based on scattering from surface nonuniformities, and includes thermochemical interactions on the surface of the material to create the grooves. This model is implemented in a simulation software that takes material, laser and scanning parameters and finds out the resulting surface structure. The simulation software is used to observe normal LIPSS on the surface of Ti and validated by normal LIPSS results. It predicts the existence of various more types of LIPSS, specifically hexagonal LIPSS, using a single scan with linearly polarized light, as demonstrated experimentally in this work. The parameters obtained in the simlation are used in fabrication to obtain hexagonal LIPSS. The desired surface structures are obtained on Ti surfaces.

Keywords: LIPSS, Surface structuring, Laser micro-nano fabrication

ÖZ

LAZER KAYNAKLI PERIYODIK YÜZEY YAPILANDIRMASININ MODELLENMESI VE SIMÜLASYONU

Yayla, Mahmut Sinan
Yüksek Lisans, Fizik
Tez Yöneticisi: Dr. Öğr. Üyesi Ihor Pavlov

Ocak 2023, 46 sayfa

Son yıllarda, lazer kaynaklı periyodik yüzey yapılandırmaya (LIPSS) olan ilgi, kullanımındaki kolaylık ve maliyet etkinliği nedeniyle artmaktadır. Geleneksel olarak kullanılan mikro ve nano yüzey yapılandırma yollarına gelecek vaadeden bir alternatiftir. Alanda genel kabul görmüş ve desteklenen teorik çalışmalar olmasına rağmen, olgunun tam bir modeli yoktur. Bu tez çalışması, yüzey pürüzlerinden saçılmaya dayalı teorik bir model sunar ve yüzey yapılarını oluşturmak için malzeme yüzeyindeki termokimyasal etkileşimleri de içerir. Bu model, malzeme, lazer ve tarama parametrelerini girdi olarak alan ve yüzey taraması sonucu oluşan yüzey yapısını bulan bir simülasyon yazılımında uygulanmaktadır. Simülasyon yazılımı, Ti yüzeyinde normal LIPSS gözlemlemek için kullanıldı ve paralel LIPSS sonuçlarıyla doğrulandı. Bu çalışmada deneysel olarak gösterildiği gibi, doğrusal olarak polarize ışıkla tek bir tarama kullanarak, çeşitli LIPSS türlerinin, özellikle altıgen LIPSS'nin varlığını tahmin eder. Simülasyonda elde edilen parametreler, altıgen LIPSS elde etmek için üretimde kullanıldu. Ti yüzeylerinde istenilen yüzey yapıları elde edildi.

Anahtar Kelimeler: Yüzey yapılandırma, lazer kaynaklı periyodik yüzey yapılandırma, lazer mikro nano üretim

Dedication to my friends and family.

ACKNOWLEDGMENTS

I would like to express my deepest gratitude to my supervisor Assist. Prof. Dr. Ihor Pavlov for his support, guidance, and insight throughout the research.

I want to thank Dr. Arian Goodarzi and Fırat İdikut for their suggestions, comments, and guidance during this research. They helped me to learn about the process and theoretical background information.

I am deeply thankful to my friends S. Emir Ogan and M. Fatih Şahin for their support and friendship since high school. I also would like to send my gratitude to Şükrü Sinan Aydoğdu, Nazlıcan Yamankurt Aydoğdu, Kubilay Yılmaz, Berkay Çiftci and M. Berat Yüksel for their never-ending support and encouragements.

This work is partially funded by Scientific and Technological Research Council of Turkey under grant number TUBİTAK 118F375.

TABLE OF CONTENTS

LIST OF TABLES

TABLES

LIST OF FIGURES

FIGURES

LIST OF ABBREVIATIONS

ABBREVIATIONS

LIPSS: Laser-Induced Periodic Surface Structuring/Structures

FDTD: Finite-difference time-domain

SPP: Surface Plasmon Polariton

HAZ: Heat Affected Zone

PPS: Pulse per Spot

HWP: Half-Wave Plate

QWP: Quarter-Wave Plate

HSFL: High Spatial Frequency LIPSS

LSFL: Low Spatial Frequency LIPSS

FWHM: Full Width Half Maximum

LIST OF SYMBOLS

SYMBOLS

ε_0: Vacuum Permittivity

ε_m: Permittivity of the material surrounding the metal

ε: Dielectric function of the metal sphere

α: Polarizability of metal nanoparticle

λ: Free space wavelength of light

Λ: Spatial wavelength or LIPSS period

δ: Optical penetration depth of the material

CHAPTER 1

INTRODUCTION

Laser-induced periodic surface structures (LIPSS) are the surface modifications that appear on the surfaces of materials in the form of periodic or quasi-periodic lines under intense short pulse laser light. They mostly appear in the form of parallel lines on the surfaces of materials with periods smaller than wavelength of incident laser. LIPSS is first obserbed by Birnbaum in 1965 [1]. They have attracted the attention of many scientists and led them to this field ever since Birnbaum's first observation [1]. After this observation, it was realized that these structures could also be formed on metal, semiconductor and dielectric surfaces [2,4-7,10,11]. However, studies are still continuing on the production of these structures on surfaces in desired shapes and in a controlled manner as pointed out by Bonse and Gräf [12]. In addition to the studies in the field of application, theoretical studies are still continuing. It is still being attempted today to arrive at a comprehensive theoretical description of the topic and to develop techniques for fabricating structures in desired forms on various materials [13].

1.1 Brief History of Modelling and Simulation of LIPSS

To totally control the surface structuring process, a complete theoretical description of LIPSS is required. Researchers developed numerous theories to explain the phenomenon. The existing electromagnetic approaches on LIPSS formation mainly focus on the scattering of light from the nonuniformities on the surface of the materials. The scattered and incident electromagnetic waves interfere with each other and resulting intensity distribution results in nonuniform energy deposition to the surface.

Following Birnbaum's discovery of LIPSS, other scientists began to investigate the phenomena [1]. Emmony *et al.* postulated that these structures emerge as a result of incident light interacting with scattered light from surface nonuniformities [16]. Their investigation is reinforced by Temple and Soileau's findings, which supported the scattering idea by inserting an induced dipole field as the source of the surface structures [31]. Surface scattering is combined with surface polaritons by Keilmann and Bai [26]. The surface scattering approach is then extended by Sipe *et al.* and the name laser induced periodic surface structuring (LIPSS) is given to the phenomenon [25]. In their study, the group also showed that the surface structures depend on the material, laser wavelength and polarization and surface roughness [25, 32].

After computational powers of the computers increased in 2000s, these methods started to be simulated. FDTD method is started to be used in the simulations of these structures and the creation of the grooves on the surfaces. The study by Skolski *et al.* includes Sipe's theory of LIPSS, and combines it with Drude model to understand the changes in refractive index of the materials under intense electric field [27]. It shows that the LIPSS periods can be calculated using FDTD methods and it supports the results found before [27].

The study by Öktem *et al.* uses the idea of induced dipole fields [25, 26, 30, 31]. Their work focuses on the interference between the dipole scattered electromagnetic waves and incident wave, the interference pattern leading inhomogeneous intensity distribution and finally to surface structuring. The simulation carried out in the study shows that structures created by the first pulse ensures the creation of LIPSS for large areas [30].

1.2 Inspection of LIPSS

Due to variations in the spatial frequency of the fabricated surface structures, the angle between the created groves on the surface and the polarization of the light, and

whether they result in surface oxidation or ablation, LIPSS may be separated into subgroups [8].

1.2.1 Spatial Frequency

We can divide laser-induced surface structures in two main groups according to their spatial frequency. These are called high spatial frequency LIPSS (HSFL) and low spatial frequency LIPSS (LSFL). The period of HSFL formed on the surfaces of materials is around one-fifth or one-tenth of the wavelength of the laser incident on the surface [8]. This ratio is close to one in LSFL. In other words, for LSFL the structures formed on the surface have spatial wavelength values close to the wavelength of the light falling on the surface. The sketch of these structures can be seen in Figure 1.1.

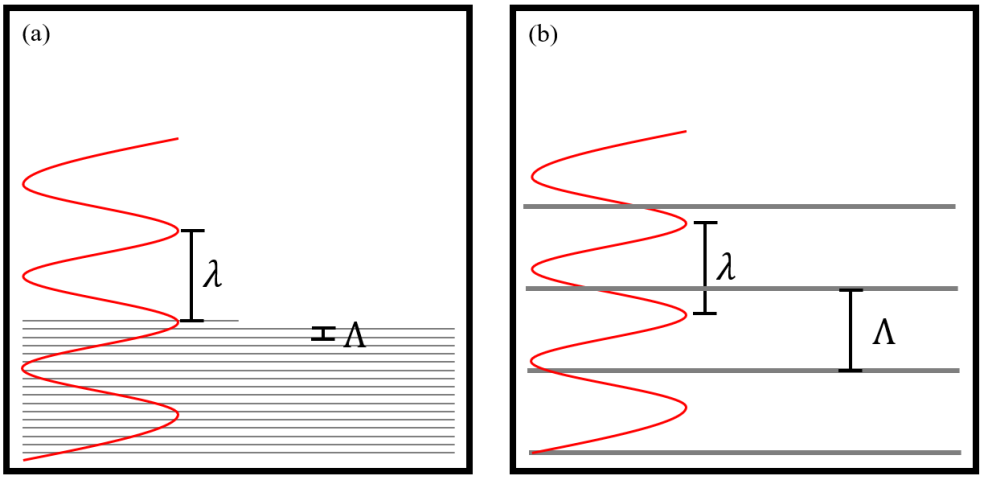

Figure 1.1. Sketch of (a) HSFL and (b) LSFL.

1.2.2 Orientation of LIPSS

LSFL can be studied in two different ways depending on the orientation of structures with respect to the polarization of the light falling on the surface. These are called normal and anomalous laser-induced surface structures. In normal LIPSS, the structures on the surface are formed perpendicular to the polarization of the laser

light incident on the surface. In anomalous LIPSS, the structures formed on the surface are parallel to the polarization of the laser falling on the surface. The drawing of the formation of these structures can be seen in Figure 1.2.

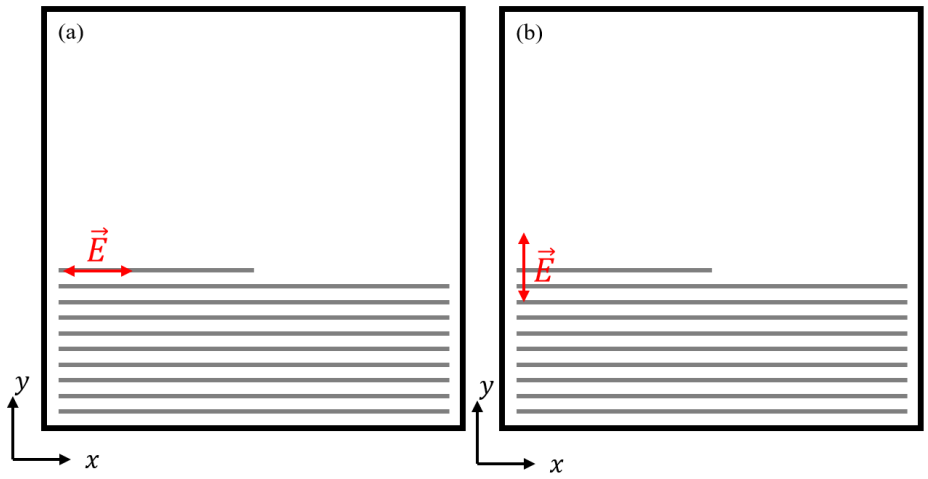

Figure 1.2. Sketch of (a) anomalous (the structures are parallel to the polarization of incident laser), (b) normal (the structures are perpendicular to the polarization of incident laser) LIPSS.

1.2.3 Structure Formation Mechanism

For the structure formation mechanism, there are two main processes involved, if the sample is illuminated in ambient air atmosphere. They are oxidation and ablation. In oxitadion, interference pattern activates (manly due to heat effect) the surface material to create bonds with the ambient O_2. In this mechanism, oxides can be created in several types of shapes. The most observed structures in this mechanism is the formation of ripples on the surface. The second mechanism that LSFL can occur is the ablation of the material which happens for the points of the surface where local intensity exceeds the ablation threshold. In ablation, the shapes created on the surface can vary depending on material, incident laser energy, scanning and jump speeds, and the angle between the polarization of incident electric field and scanning velocty vector. Examples of structure formation by oxide formation and ablation are shown in Figure 1.3 [9]. Figure 1.3 demonstrates an example of anomalous oxidation

LIPSS (a) which orientation is parallel to the polarization of the incident light, and normal ablation LIPSS (b) with the direction of the groves perpendicular to the polarization of the incident light.

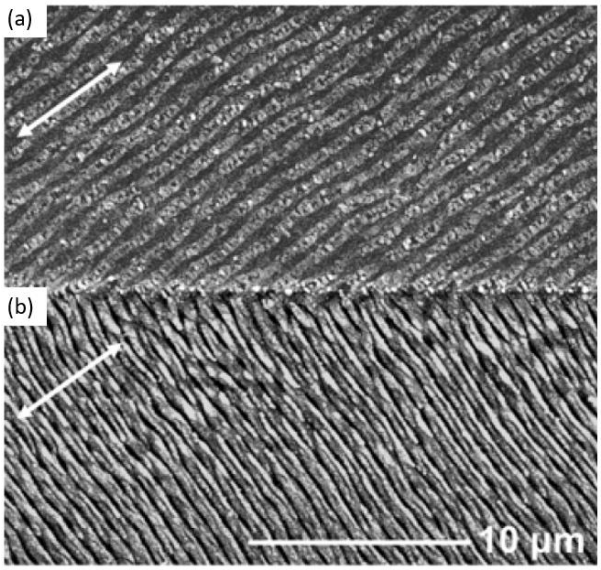

Figure 1.3. (a) Anomalous oxidation LIPSS formed on Ti surface, (b) normal ablation type LIPSS formed on the same surface [9].

Throughout this thesis, low spatial frequency laser induced periodic surface structuring will be studied. Although the software is capable of simulating both anomalous oxidation and normal ablation, the main focus is on normal ablation type LIPSS, i.e. they will be formed perpendicular to the incident laser polarization.

1.3 Objective of This Work and Organization

In this thesis, investigation of the formation of different structures under different laser parameters (scan speed, polarization, pulse overlap) will be done by theoretical modelling and experientially. The theoretical model and simulation of the structure formation will be studied and a custom-made femtosecond pulsed fiber laser that produces 300 fs pulses that peaks around 1030 nm will be used in the experimental work carried out in the study. Scanning parameters will be found in simulation and optimized in experiment to obtain the hexagonal LIPSS with linearly polarized light

by a single scan. Although these types of surface structures can be obtained with different laser polarizations and multiple scanning, this study will show that it can be achieved by a single scan with linearly polarized light. Simulation and fabrication of the structure formation will be inspected.

In Chapter 2, Theory, the structure formation mechanism is inspected in detail by starting with the electromagnetic phenomena occurring on the surface of metals, the interaction between the laser light and the nonuniformities on the surface and creation of surface-scattered waves. Then, the ablation process with which the material is removed from the surface will be shown. The mechanism is studied first by introducing an ablation heat capacity, then by combining it with optical penetration depth to calculate an intensity and energy threshold. Lastly, the effect of scanning parameters such as scanning speed, jump distance and polarization of incident laser light is shown.

After establishing the fundamentals of LIPSS, the simulation of the structures is presented in Chapter 3. First, there is an explanation of the surface-scattered wave calculation. Then, surface structure formation is introduced by the inspection of oxidation and ablation processes, after that the implemented formulas are given. Before moving on to the simulation results, the laser beam path creation is explained shortly. In the last part of simulation chapter, the results of the numerical calculations and simulated surface structures are presented.

Chapter 4, Fabrication of Surface Structures, detailed information about the femtosecond laser setup is presented. After that, the preparation of samples and the fabricated surface structure are shown. The SEM images of the surface structures are presented and LIPSS periods are presented using these SEM images.

In the last chapter, the 5th chapter, the results obtained in this research are summarized. Their implications in LIPSS research is given and the work that needs to be done in order to reach the conclusion of this research is presented.

CHAPTER 2

THEORETICAL BACKGROUND

2.1 Introduction

Surface modifications at the nanometer scale can be achieved in many ways. An alternative method to surface structuring is laser-induced periodic surface structuring (LIPSS), which offers an cost-effective and simple way to obtain the desired surfaces. The theory of LIPSS can be inspected in two main sub-topics, electromagnetic and thermal interaction between the surface and the incident electric field.

The electromagnetic phenomena that govern the LIPSS generation process have been of interest since its first observation by Birnbaum [1]. Emmony *et al.* suggested in 1973 that the LIPSS are generated by the interference of incident laser beam with the surface-scattered waves [16]. They thought that the nonuniformities on the surfaces of materials acted as point sources of electromagnetic waves which resulted in a periodic interference pattern [16]. After that, Sipe *et al.* published their theory on the generation of LIPSS [25]. Their theory predicted the possible LIPSS wave vectors of the surface as a function of laser and surface parameters. The energy deposition pattern on the surface is proportional to an efficacy factor and the surface roughness function. The study of Sipe and coworkers included the dependence of surface-scattered waves' on laser polarization, wavelength, angle of incidence and wave vector, and surface parameters such as dielectric permittivity and surface roughness [25].

In this study we focus on the method first put forward by Emmony *et al.* which states the scattering of light from the surface nonuniformities to understand the

electromagnetic interaction [16, 31]. Similar approach was applied in numerical simulation by Oktem *et al.,* however with only far field dipole scattering included [30]. To understand and model the thermochemical interactions the study by Gamaly and Nolte are used [21,22]. The study mainly describes a phenomenological approach to the problem.

They will be inspected in the following topics;

1. Light scattering via non-uniformities on the surface,
2. Structuring on the surface due to this energy deposition and governing principles,
3. Effect of scanning parameters.

2.2 Light Scattering via Non-Uniformities on the Surface

On the surface of a metal (in most of the cases we will consider Ti in this work), there are inherent nonuniformities that scatter the incident electric field. The interaction between nonuniformities and incident electric field can be seen as dipole scattering. Assuming that the incident laser is as in Equation 2.1,

$$E_{inc} = E_0 \exp(\vec{k}.\vec{x} - \omega t) \tag{2.1}$$

where E_0 is the amplitude of the electric field, k is free space wavenumber, and ω is the angular frequency of the incident electric field. In reality, the laser has a transverse Gaussian distribution. Hence, E_0 includes the transverse distribution of the laser. Assuming the laser propagates in the z-direction, E_0 can be written as in Equation 2.2,

$$E_0 = |E_0| \exp(-(\frac{(x-x_0)^2+(y-y_0)^2}{2w^2}) \tag{2.2}$$

where (x_0, y_0) pair is the center, and w is spot size of the laser. Incident laser distribution can be seen in Figure 2.1.

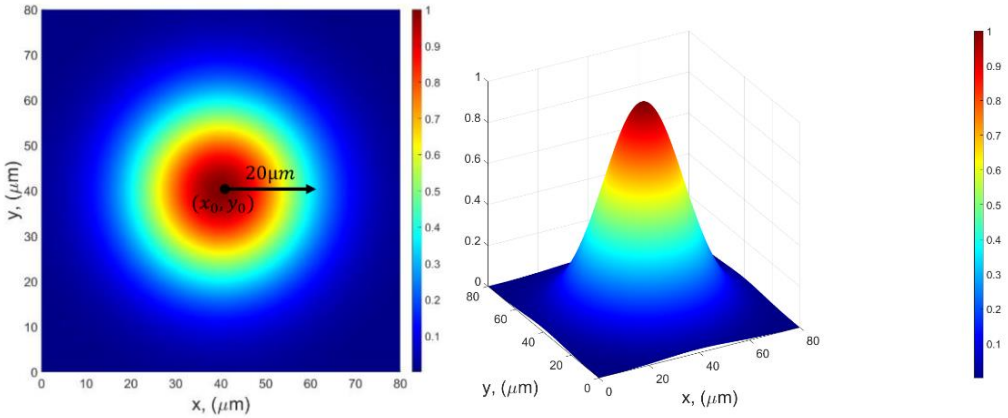

Figure 2.1. Incident laser intensity distribution, spot size is 20 μm.

To completely model and inspect the surface of a metal is complicated, and the computational power it needs to be carried out is enormous. To ease the task at hand, the interaction between the incident laser and the nonuniformities on the surface can be modelled as scattering from a spherical particle which is shown in Figure 2.2.

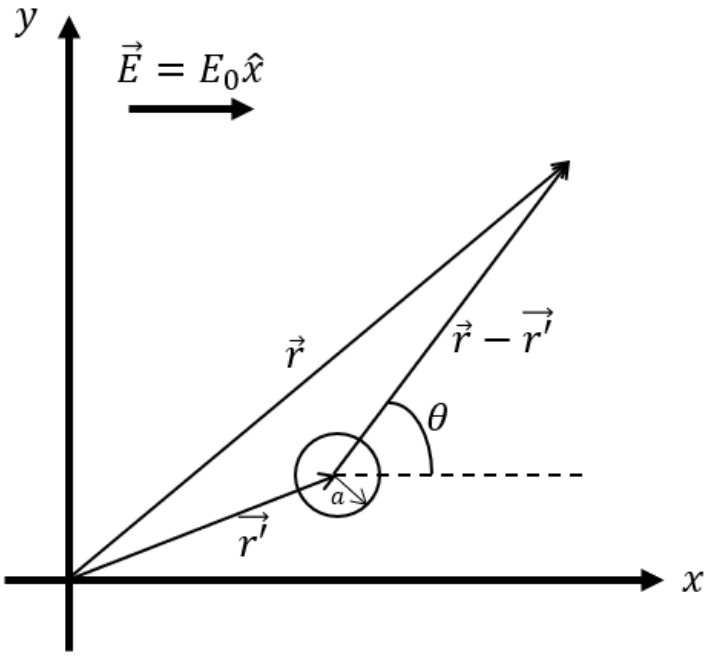

Figure 2.2. Sketch of a homogeneous sphere with radius a, placed into an electrostatic field in x-direction.

The electric field present around the metal sphere with radius a induces a dipole as in Equation 2.3[3,23];

$$\vec{p}(t) = \epsilon_0 \epsilon_m \alpha \overrightarrow{E_0} e^{-iwt} \tag{2.3}$$

Here, ϵ_m is the dielectric function of the surrounding material, α is polarizability that is defined as [3,23];

$$\alpha = 4\pi a^3 \frac{\epsilon - \epsilon_m}{\epsilon + 2\epsilon_m}$$

For an oscillating dipole, the scattered electric field can be written as in Equation 2.4 [3];

$$\vec{E} = \frac{1}{4\pi\epsilon_0\epsilon_m}\{k^2(\vec{n} \times \vec{p}) \times \vec{n}\frac{e^{ikr}}{r} + [3\vec{n}(\vec{n}.\vec{p}) - \vec{p}]\left(\frac{1}{r^3} - \frac{ik}{r^2}\right)e^{ikr}\} \tag{2.4}$$

In Equation 2.4, the first term in parenthesis defines the dipole far field since it has a first-order dependency on the radial distance from the scatterer. The second term has 2nd and 3rd-order dependencies on the distance from the scatterer, hence it can be called as a near-field component. These fields are created at different angles with respect to the x-axis shown in Figure 2.2. The dipole field far field depends on cosine function whereas the near field depends on sine function, meaning that for the dipole induced by an incident electric field in the x-direction, the far field is around the x-axis, and for the near field is in around the y-axis.

2.2.1 Near Field

On the surface of the metal, nonuniformities scatter the incident electric field. During scattering on the surface, the spikes on the surface act as dipoles. As we know from dipole scattering, the process follows Equation 2.5 in the near field [3];

$$\vec{E}_{near} = \frac{1}{4\pi\epsilon_0\epsilon_m}[3\vec{n}(\vec{n}.\vec{p}) - \vec{p}]\left(\frac{1}{r^3} - \frac{ik}{r^2}\right)e^{ikr} \tag{2.5}$$

In the equation, k represents the free space wavenumber, n is the unit vector in the direction of observation, and r is the distance from the scatterer.

The induced field due to the incident electric field in the x-direction can be found as in Equation 2.6;

$$\vec{E}_{near} = 3\frac{\epsilon-\epsilon_m}{\epsilon+2\epsilon_m}a^3(\cos^2\theta\,\hat{x} + \cos\theta\sin\theta\,\hat{y})(\frac{1}{r^3} - \frac{ik}{r^2})e^{ikr}E_0 \qquad (2.6)$$

Here, E_0 is the amplitude of the incident electric field, and θ is defined as the angle between the polarization direction and the unit vector of the vector connecting the center of the dipole and observation point, $\hat{n}$ is the said unit vector in the direction of observation. From here, it can be seen that the incident electric field in the x-direction induces an electric field in the x-direction dependent on cosine function that can interfere with itself.

2.2.2 Far Field

In addition to the near field, a far-field component is generated due to the induced dipole. The equation defining the far-field component can be written as in Equation 2.7;

$$\vec{E}_{farfield} = \frac{1}{4\pi\epsilon_0}\frac{e^{ikr}}{r}((\vec{n}\times\vec{p})\times\vec{n})) \qquad (2.7)$$

Solving this equation for the incident electric field in the x-direction, the generated field can be found as shown in Equation 2.8;

$$\vec{E}_{farfield} = \frac{\epsilon-\epsilon_m}{\epsilon+2\epsilon_m}a^3\frac{k^2}{r}(\sin^2\theta\,\hat{x} + \cos\theta\sin\theta\,\hat{y})e^{ikr}E_0 \quad (2.8)$$

From here, it can be seen that the generated field has a component in the x-direction that is dependent on sine function.

2.2.3 Combination of the Surface Induced Fields and Their Interference with the Incident Light

The fields generated due to the scattering from the surface nonuniformities interfere with the incident electric field while generating the grooves on the surface. These grooves follow the interference pattern created on the surface. Depending on the energy of the incident field and the material, the dominant field component changes for the generated fields on the surface. In ablation LIPSS, the intenstiy of the laser light hitting on the surface is large; hence, the interference pattern observed on the surface is mainly dominated by the near field effects described in Section 2.2.1. Due to that, the resulting interference pattern on the surface is perpendicular to the polarization of the incident electric field.

As shown in Section 2.1.1 and 2.1.2 the generated fields due to the incident electric field have components in x and y directions, one of which does not interfere with the incident electric field. For the sake of simplicity, the calculation of the scattered field along the x-direction, the one that can interfere with the incident electric field, will be inspected in this part.

By combining the Equation 2.6 and 2.8 we can get the resulting scattered field in the x-direction as in Equation 2.9;

$$\vec{E}_{scattered} = \frac{\epsilon-\epsilon_m}{\epsilon+2\epsilon_m} a^3 \{\frac{k^2}{r} \sin^2\theta + 3\cos^2\theta \left(\frac{1}{r^3} - \frac{ik}{r^2}\right)\} e^{ikr} E_0 \hat{x} \quad (2.9)$$

As it can be seen from here, there is a third-order dependency on the radius of the sphere described in Figure 2.2. On the simulated surface, the third-order dependency on the radius shown in Equation 2.9 has been replaced by the height of the cell and the step size to calculate the scattered electric field on the material surface. This modification is shown in Equation 2.10 (see Figure 3.3 for space step);

$$\vec{E}_{scattered} = \frac{\epsilon-\epsilon_m}{\epsilon+2\epsilon_m} (h * spaceStep^2) \{\frac{k^2}{r} \sin^2\theta + 3\cos^2\theta \left(\frac{1}{r^3} - \frac{ik}{r^2}\right)\} e^{ikr} E_0 \hat{x} \quad (2.10)$$

The calculation of the effect of every point on the surface is found as in Equation 2.11;

$$E_{scat}(x,y) = \frac{\epsilon-\epsilon_m}{\epsilon+2\epsilon_m}\iint E_0(x',y')h(x',y')(\frac{k^2}{r}\sin^2\theta + 3\cos^2\theta\left(\frac{1}{r^3} - \frac{ik}{r^2}\right))e^{ikr}dx'dy' \quad (2.11)$$

Then, in order to find the total electric field, Equation 2.12 is carried out;

$$E_{total} = E_{inc}(x,y) + E_{scattered}(x,y) \quad (2.12)$$

The resulting field deposits the energy incident wave carries in a certain pattern, which results in the surface profile changing in an orderly fashion. This resulting field is then used as the height of the surface.

For the case of ablation with normal LIPSS formation, the governing process is thought to be surface plasmon polariton waves. This model is used in order to explain the scattering mechanism, and it is used in several well-respected publications in order to explain surface plasmon polaritons caused by metal nanoparticles [19,20].

2.3 Energy Deposition and Surface Profile Modification

Surface modification in LIPSS depends on the laser parameters and the material used in the process. Laser parameters that affect the process are pulse length, laser wavelength, and pulse intensity. On the other hand, the material properties that have significant importance in the process are electric permittivity, heat capacity, and phase change energies.

The laser wavelength and electric permittivity of the material directly decide the optical penetration depth of the material (δ). Absorption of the electric field inside the material is described by an absorption coefficient α, which is shown in Equation 2.13;

$$I(z) = I_0 e^{-\alpha z} \quad (2.13)$$

where, I_0 is the incident intensity, and z is the distance travelled inside the material. Here, the absorption coefficient (α) depends on the imaginary part of the dielectric function of the material. The material used in this study is Titanium. The value of the dielectric function at the wavelength we work (1030nm) is $\epsilon(\lambda)_{\lambda=1030nm} = -4.2656 + i27.277$ [15]. From here, the refractive index of Ti at 1030 nm is calculated to be $n + i\kappa = 3.41 + i3.9921$ [15]. Using these values, the optical penetration depth (δ=1/α) shown in Equation 2.13 in Ti at 1030 nm is approximately 20 nm.

The optical penetration is insufficient to model the profile modification process in LIPSS. To completely understand the process, it is a must to inspect the heating and phase change of the material. Assuming that the material is initially at room temperature, its temperature increases to boiling temperature. The laser must supply the energy needed to obtain this. This energy value is calculated as the combination of the energy needed to increase the material temperature and phase change energies. The total energy that is needed is shown in Equation 2.14;

$$E_{need} = E_{heating} + E_{melting} + E_{boiling} \tag{2.14}$$

using the values for Ti, the amount of energy to ablate 1 g of material can be calculated as 10880 J/g. The intensity that is needed to ablate Ti for 30 nm thickness can be calculated as 0.0981 J/cm^2. The value is close to the literature value [17,18]. This value is used in simulations as the threshold to obtain the resulting structures.

Another important point in the process and simulations is that the laser pulses do not overlap with each other. The pulse length is around 300 fs and the pulse rate is 1 MHz. Hence, there is approximately 1 μs difference in time between pulses. The main result of pulse length and pulse rate is that the pulses can be inspected as individual processes. The length of the pulses is smaller than that of conductive heat transfer in the material, which happens at the orders of nanoseconds that cannot happen during the laser pulse duration, creating small heat-affected zones (HAZ). Having small HAZ means that laser–material interaction does not result in residual nonuniformities on the surface of the material. The pulse rate or the time between

each pulse ensures that the heating effect of each pulse does not overlap, meaning that the thermal interactions are separated. The portions on the surface that interacted with the incident laser can cool down during the time between pulses which makes the initial conditions for each pulse the same.

The height change on the surface is calculated using the energy or intensity threshold calculated in Equation 2.14. The depth of the heat affected volume can be calculated using Equation 2.15 [21,22];

$$h_{affected} = (log\left(\frac{I_{tot}}{I_{th}}\right))/\alpha \tag{2.15}$$

Here, α is the absorption coefficient, I_{tot} is the total electric field after the interference, and I_{th} is the threshold intensity. The affected depth vs intensity graph by using the formula given above can be observed in Figure 2.3.

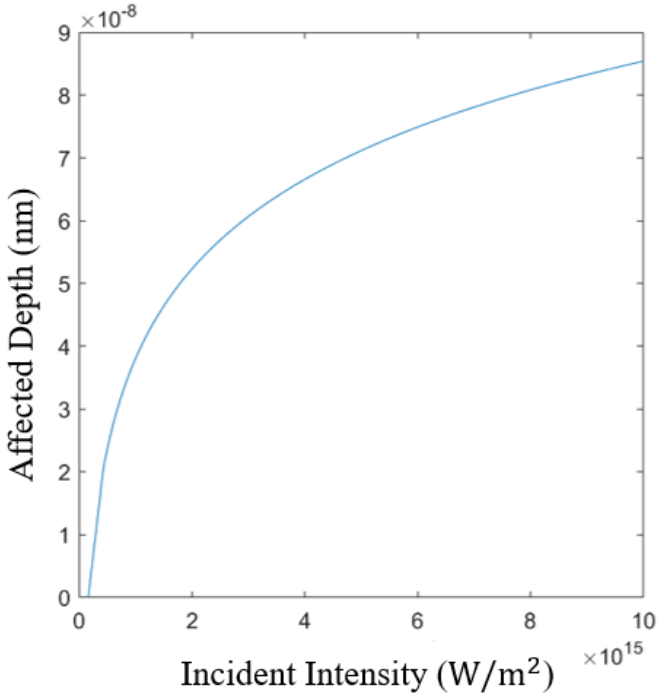

Figure 2.3. Affected depth vs. Incident Intensity, effected depth is calculated using Equation 2.15.

2.4 Scanning Parameters

The parameters that are available in the setup are scanning speed, jump distance, and polarization angle. Scanning speed is the value at which the laser moves on the surface. The jump distance is the distance between the lines where the scanning takes place. The polarization is the laser polarization. The changes in these parameters affect the output structure that is created in LIPSS.

The scanning speed and jump distance decide the number of pulses per area on the surface. The number of pulses per area is one of the main factors while creating surface structures.

The angle between the laser scanning velocity and polarization of incident laser light changes the orientation of the created structures on the surface. In addition to those two, the jump speed also affects how the structures are created. The sketch of these parameters is shown in Figure 2.4.

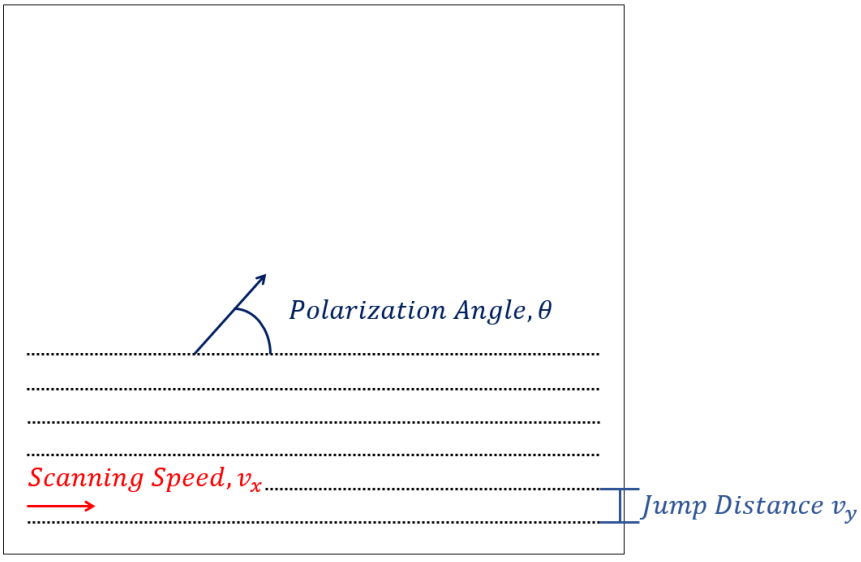

Figure 2.4. Sketch of scanning parameters on sample surface, polarization degree is the angle between the scanning speed and incident light polarization, scanning speed is the speed at which the surface is scanned, jump distance is the distance between equidistance lines that are scanned by the laser.

The pulse per spot (PPS) changes with the scanning and jump distance. The radius of the incident intensity is calculated as the radius at which the intensity decreases to 1/e of the maximum intensity. PPS is calculated as the number of pulses whose centre is located inside the first pulses radius. As an example, for an intensity distribution of $r = 10\ \mu m$ and scan and jump speeds of $4\ m/s$ with 1 MHz repetition rate, there are 21 pulses per area. The sketch of the location of the first two pulses falling on the same location is shown in Figure 2.5.

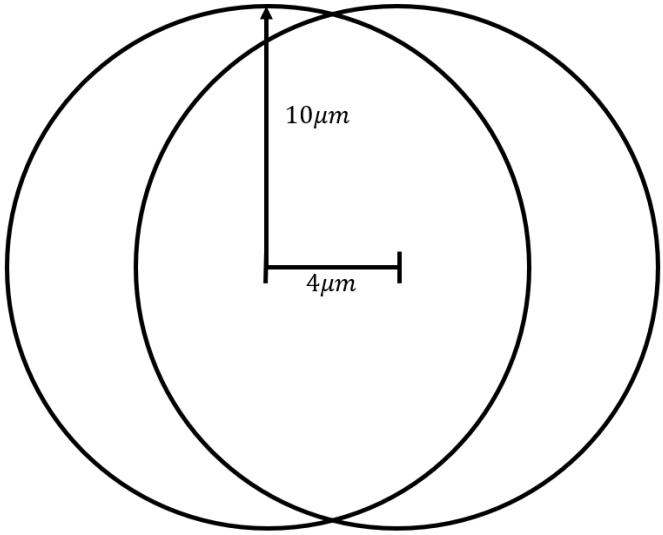

Figure 2.5. Pulses on the same location.

CHAPTER 3

SIMULATION OF LIPSS CREATION PROCESS

3.1 Introduction

This chapter explains the simulation code's working principles and shows the selected output surface profiles. The simulation of the LIPSS based on the theory described in Chapter 2. The electric field is calculated by following the equations in Section 2.1. Then, the surface profile is modified using the electric field on the surface. Different calculation methods are used for different mechanisms that happen on the surface for the creation of LIPSS. For oxide creation on the surface, the affected material depth is calculated, then it is converted to oxide, and the new height is found. For ablation, the affected material depth is taken out of the surface, and the new depth is saved for new structure formation. The source distribution is calculated on every timestep since the center of the laser distribution moves on the surface. The path that the beam follows is decided at the beginning of the simulation, depending on input parameters.

This chapter will start with the surface profile creation, and the parameters needed to define the surface profile will be presented. The surface profile modification will be followed by defining the laser beam distribution and the parameters that it depends on. After defining the surface profile and laser distribution on the surface, surface–incident electric field interaction, the scattered field calculation, and interference of this scattered field with the incident field will be given. The surface modification will be presented in detail following the electromagnetic field calculations. Oxide creation and ablation of the material will be explained separately. To understand the effect of the material, ablation threshold calculation is going to be introduced. The explanation simulation will be finished with the path that the laser

travels during the process. After finalizing the inspection of the simulation code, several results will be given.

3.2 Surface Profile Creation

The surface profile is created depending on the desired structure creation mechanism. There are two ways to create the surface profile: the randomized surface profile, the surface with a single defect. The randomized surface is used in both oxidation and ablation simulation types. However, the single defect surfaces can only be used in oxide creation simulations. For LIPSS creation via ablation, the randomized surface is needed. Otherwise, the surface structuring only occurs near the single defect defined on the surface.

To create the initial surface profile, the following parameters are needed;

1. The limits of the surface,
2. The minimum cell size or space step,
3. Maximum defect height,

These parameters are the fundamental inputs that both surface types require. The limits of the surface define the size simulated surface. The space is divided into a grid with minimum cell size (space step) distance between the lines. The maximum defect height is used differently for randomized and single-defect surfaces. For randomized surface profile, it defines the maximum height of the nonuniformities on the surface. For the single defect case, it defines the height of the defect. The surface type decides whether the randomized or single defect surface is created.

The following sections will give an example input and output set for randomized and single-defect surfaces. The randomized surface will be created for ablation simulation, and the single defect surface will be for oxide creation simulation.

3.2.1 Randomized Surface

For the randomized surface, no additional inputs other than the fundamental ones are needed. A random number generator creates the surface profile that takes its values from the standard normal distribution. The randomized surface mode generates only the material surface. The sample surface is shown in Figure 3.1.

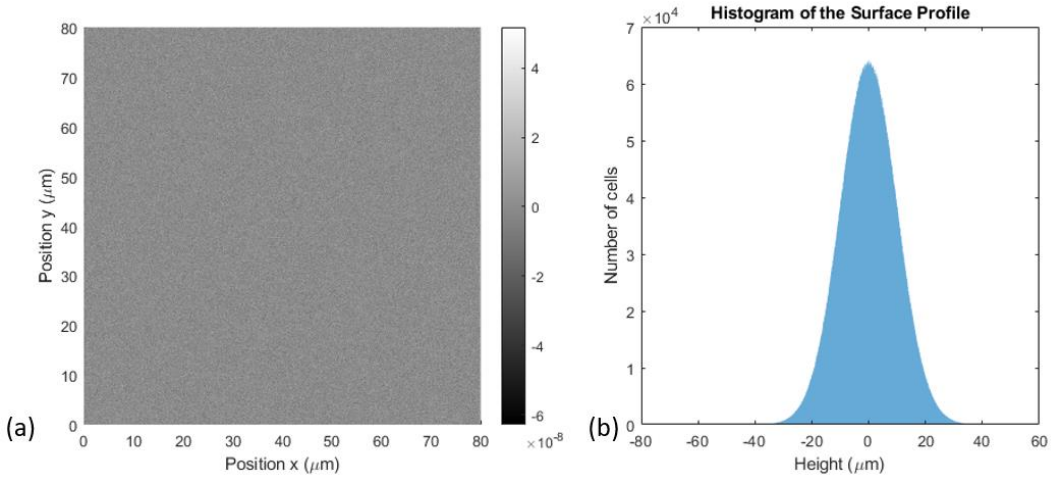

Figure 3.1. (a) Sample surface for random surface generator, (b) histogram of the surface height.

3.2.2 Surface with Single Defect

For several special cases a single defect on the surface is useful. For example, while inspecting validity of the scattered field profile, it is important to use a single point nonuniformity as the source of scattering.

The defect radius is needed in addition to fundamental inputs to create a surface with a single defect. The defect radius decides the size of the nonuniformity created on the material's surface. An example surface is shown in Figure 3.2.

This mode creates three different height data for the oxide creation: oxide, material, and total heights. The electric field calculations are carried out by using the total

height. The other two, material and oxide heights, are used to create a feedback mechanism to stop the material-oxide change and follow the changes in both.

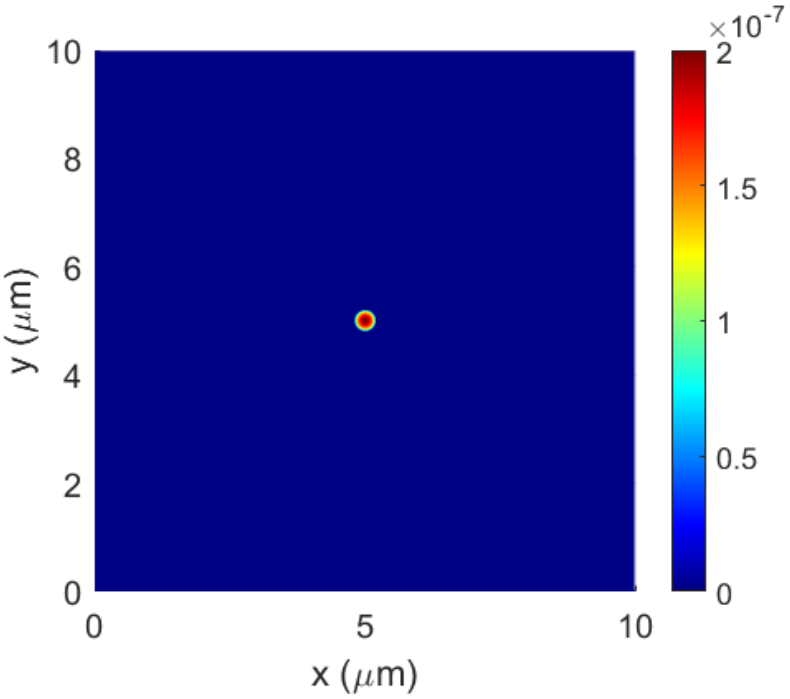

Figure 3.2. Sample surface with a single defect, the maximum height of the nonuniformity is 200 nm, the radius of nonuniformity is 200 nm.

3.3 Source Creation

The laser distribution in the transverse plane is assumed to be a fundamental Gaussian mode as mentioned in Chapter 2. In addition to that, the laser is always assumed to be linearly polarized. Hence, there is no phase difference defined in the simulation. The main parameters to define the laser intensity distribution are;

1. Maximum intensity (I_{max})
2. Polarization (ϕ_{pol})
3. Beam width (w)
4. Position of the center of the beam ($cent_x, cent_y$)

The maximum intensity, beam width, and position of the centre of the beam are used to calculate the intensity distribution of the laser. This calculation is shown in Equation 3.1.

$$I(x,y) = I_{max} e^{-\frac{(x-cent_x)^2+(y-cent_y)^2}{w^2}} \quad (3.1)$$

After calculating the intensity distribution, the laser's polarization is used to calculate the electric field distribution x and y directions. The electric field components along the x and y directions are calculated using Equation 3.2;

$$E_x = \frac{sqrt(I_{inc})}{cn\epsilon_0/2}\cos(\phi_{pol}) \quad (3.2)$$

Here, ϵ_0 is vacuum permittivity, c is the speed of light, n is the refractive index, and ϕ_{pol} is the polarization angle that can be calculated as shown in Equation 3.3;

$$\phi_{pol} = |\frac{\overrightarrow{E_x}}{\overrightarrow{E_x}+\overrightarrow{E_y}}| \quad (3.3)$$

3.4 Electromagnetic Field Calculation

The electromagnetic field calculations for near and far fields are carried out separately. In both calculations, there is a dependence on the dimensions of the surface nonuniformity. This dependence is converted to a linear one as described in Section 2.1.3. The Equation 2.6 and 2.8 that describes the near and far fields are converted to Equations 3.4 and Equation 3.5.

$$\vec{E}_{near} = 3\frac{\epsilon-\epsilon_m}{\epsilon+2\epsilon_m}(h \times spaceStep^2)(\cos^2\theta\,\hat{x} + \cos\theta\sin\theta\,\hat{y})(\frac{1}{r^3} - \frac{ik}{r^2})e^{ikr}E_0 \quad (3.4)$$

$$\vec{E}_{farfield} = \frac{\epsilon-\epsilon_m}{\epsilon+2\epsilon_m}(h \times spaceStep^2)\frac{k^2}{r}\,(\sin^2\theta\,\hat{x} + \cos\theta\sin\theta\,\hat{y})e^{ikr}E_0 \quad (3.5)$$

The height of the cell, and space step in Equation 3.4 and 3.5 are shown in Figure 3.3.

The effects described in Equation 3.4 and 3.5 are for a single scatterer on the surface. To get the effect of the whole surface on one point on the surface, there needs to be an integral scanning the surface. Hence, the total field calculation becomes a surface integral that has the height and electric field of a point act like a source, and the rest becoming an observation point dependent function. Then, the integral becomes a convolution that can be calculated by using Fourier Transformation.

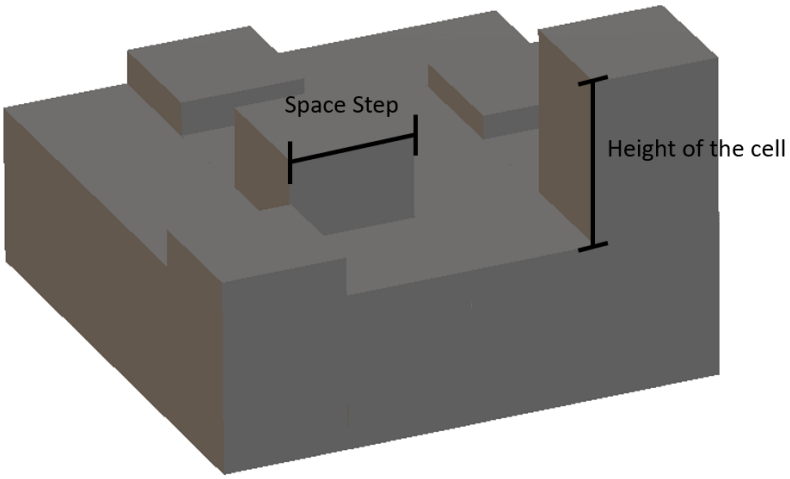

Figure 3.3. Drawing that shows the cell height, space step, the height of the cell is decided in surface creation function, the space step is one of the fundamental inputs.

3.5 Laser Beam Path Creation

The laser scans the surface during the fabrication of LIPSS. In order to create the path that the laser travels during the process, surface scanning velocity and line distances are required. These are the fundamental inputs for the structure creation simulation. In addition to the parameters that are related to the fabrication, the scanning type needs to be defined for the simulations. The defined scanning types are line, raster, and skewed raster scanning.

The surface scanning velocity is the speed at which the laser will travel on the surface. The line distance defines the distance between the two lines in the direction perpendicular to the scanning direction. The scanning type defines the shape of the

surface scanning pattern. In line scanning, there is one line that the laser moves on. The laser scans the surface on parallel equidistance lines for the raster scan. The surface scanning pattern for the skewed raster scan is similar to that of the raster scan. In the skewed raster scan, the points at which the laser hits the surface are not in line in the direction that is perpendicular to the scanning direction. Different scanning types are shown in Figure 3.4.

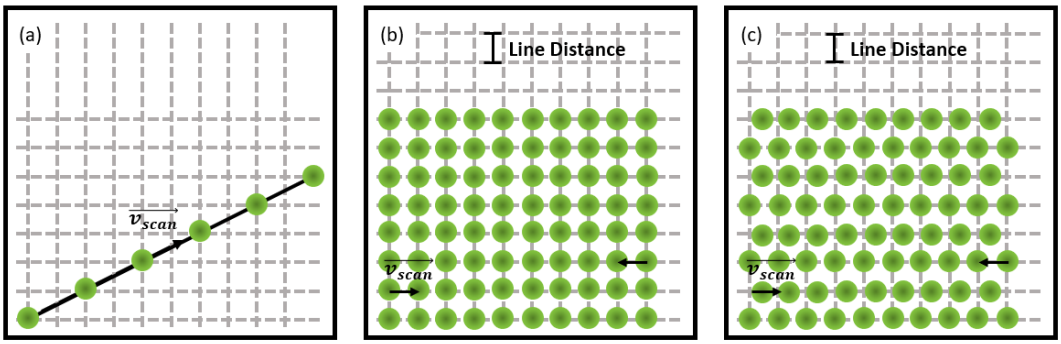

Figure 3.4. Scanning types; (a) line, (b) raster, (c) skewed raster.

3.6 Surface Profile Modification

Surface profile modification is the one of the two fundamental processes in LIPSS simulations. It has two different types of surface modification mechanisms. The first one is oxide creation, which happens when the chemically activated atoms starts interacting with ambient O_2. The second mechanism is ablation that this study focuses on. Ablation happens when the energy deposited on the surface is larger than the energy needed to heat, melt and boil the material. The calculation method and the value of this energy and corresponding intensity are defined in Section 2.2.

3.6.1 TiO_2 Creation

In order to calculate the created oxide volume and the new surface height, the heat affected volume of Ti on the surface is calculated first. The heat affected depth in Ti surface is calculated by using Equation 2.10, then using the mesh size (space step)

the volume of the affected Ti is calculated. This volume is then converted to TiO_2 using a conversion coefficient which is shown in Equation 3.6 [30];

$$Conversion\ Coefficient = \frac{d_{Ti}}{d_{TiO_2}} \times \frac{MolarMass_{TiO_2}}{MolarMass_{Ti}} \tag{3.6}$$

The height of TiO_2 generated on the surface of the material is limited by the amount of O_2 that can penetrate the created TiO_2 height. A critical value for the increase in height is defined to be $50\,nm$. The actual effected depth, i.e. the height that is converted to TiO_2 is calculated as in Equation 3.7 [30];

$$depth_{effected} = depth_{Ith} * e^{-\frac{h_{ox}}{h_{critical}}} \tag{3.7}$$

The structuring parallel to the polarization of incident laser on the surface of the material is shown in Figure 3.5. The surface in the simulation result shown in Figure 3.5 is randomized with a maximum surface roughness around 20 nm.

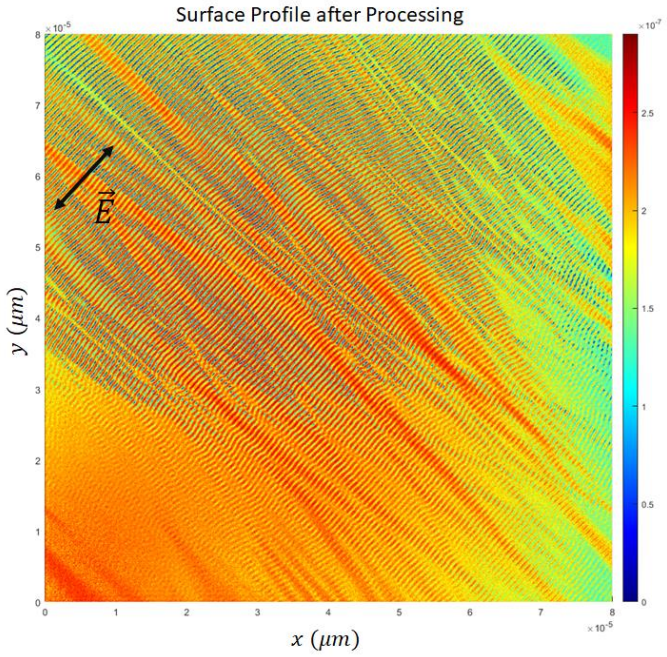

Figure 3.5. Simulation of Anomalous LIPSS created on the surface of Ti, polarization the scanning speed is 5 m/s, jump distance is 5 μm the polarization is 135 degrees as shown in the figure with the black arrow, the created structures are parallel to the incident laser.

3.6.2 Ablation on the Surface

The ablation is the removal of material from a surface. In LIPSS, this occurs at regions with an incident threshold that is larger than the energy defined in Equation 2.9. The affected depth inside the material can be calculated using this energy value. In order to decrease the simulation time, intensity that is needed to ablate 1nm of material is calculated and used as a threshold. The depth of the ablated regions is calculated using Equation 2.10 in the simulations. Result of structuring on the surface is shown in Section 3.7.

3.7 Created Surface Structures

The simulation code is used in order to predict LIPSS on Ti. The scanning parameters and polarization is modified to obtain several results. Selected simulation is given in Figure 3.6,

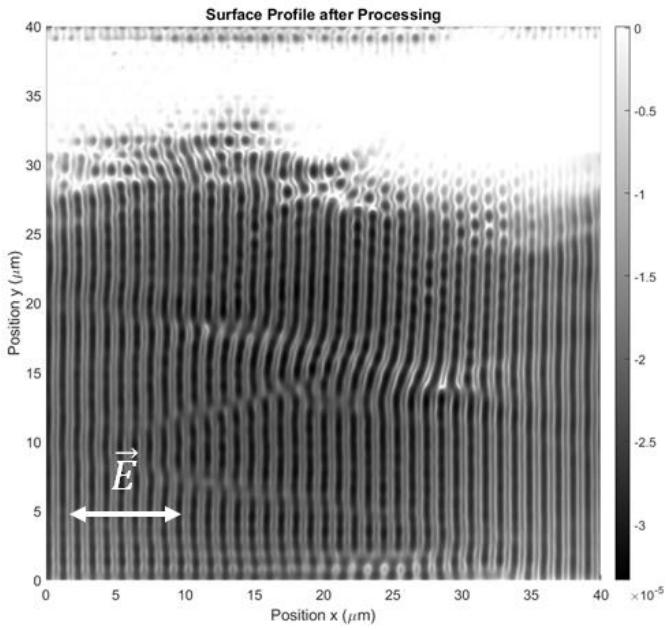

Figure 3.6. Simulation result for x-polarized incident laser, the scanning occurs in x direction, the normal LIPSS, $\vec{E}$ represents the polarization of incident laser light, parallel lines created on the surface are perpendicular to the laser polarization, laser radius on the surface is 20 μm, the scanning speed is 5 m/s, jump distance is 5 μm.

This simulation result shows when incident laser is polarized in x-direction, scanning direction is in x. The structures are created perpendicular to the incident laser polarization. During this simulation, the parameters is as shown in Table 3-1.

Table 3-1. The parameters used in the simulation of the structure shown in Figure 3.6.

Radius of laser on the surface	Scanning Speed	Jump Distance	Polarization
20 µm	5 m/s	5 µm	0° (x-pol)

3.7.1 Hexagonal LIPSS

After validating the simulation software with normal LIPSS simulations, surface scanning parameters are changed to search for different surface structures. The polarization angle, scanning speed and jump distance are scanned between certain values to check whether it is possible to obtain surface structures other than parallel lines. During this search, it is observed that the surface structures mostly appear in the form of parallel lines whose orientation is perpendicular to the laser polarization direction.

At certain surface scanning speeds, it is observed that surface structuring started to deviate from parallel lines. They started to form 2D periodic surface structures. These structures are normally expected to occur with different polarizations (circular or elliptical) or with multiple scans on the surface. An important result was the observation of hexagonal surface structures. These structures started to appear when scanning speed, jump distance and polarization angle are at certain values given below in this chapter. In the simulations of the structures, it is observed that the hexagonal structuring on the surfaces of the materials with linearly polarized light is possible. Simulation results for this type of structuring is shown in Figure 3.7 and Figure 3.8.

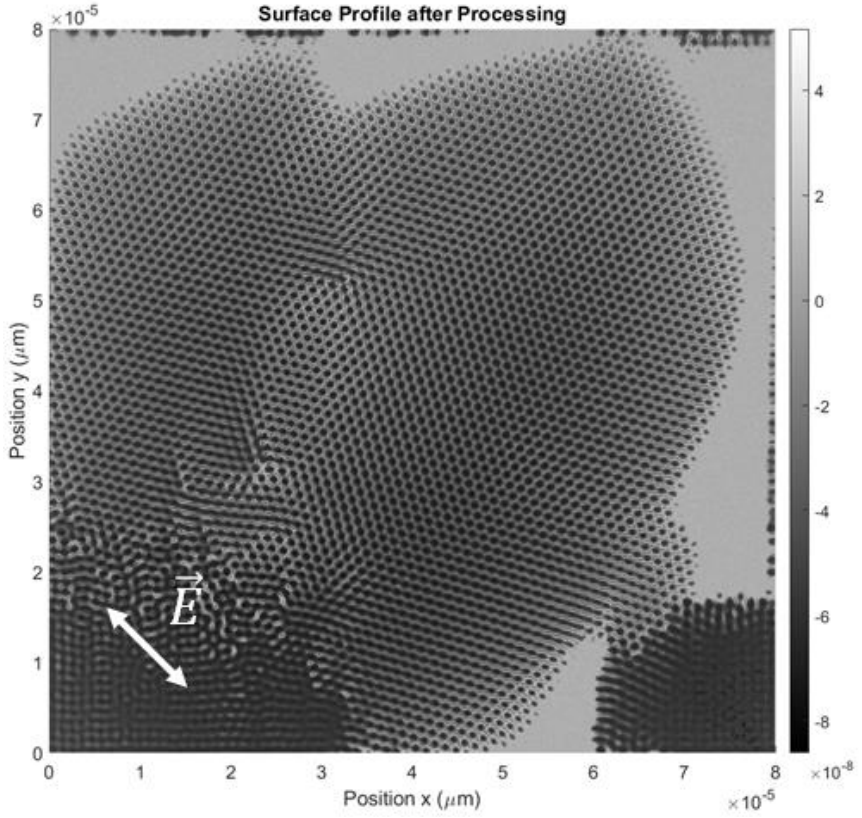

Figure 3.7. Simulation result of 45 degrees polarized light, $\vec{E}$ represents the polarization of incident laser light, scanning occurs in x direction, normal LIPSS, laser radius on the surface is 20 μm, scanning speed is 2.5 m/s, jump distance is 2.4 μm.

The surface scanning was carried out in the x direction, and the profile formed on the surface took a hexagon-like appearance. The scanning speed of the surface is 2.5m/s in the x direction. The distance between the scanning lines, that is, the jump distance, is 2.5 μm. The polarization of light is 45 degrees. The spatial wavelength or the period of LIPSS is approximately $0.9\mu m$. Up-right part of the surface structuring shows hexagonal like structuring clearly.

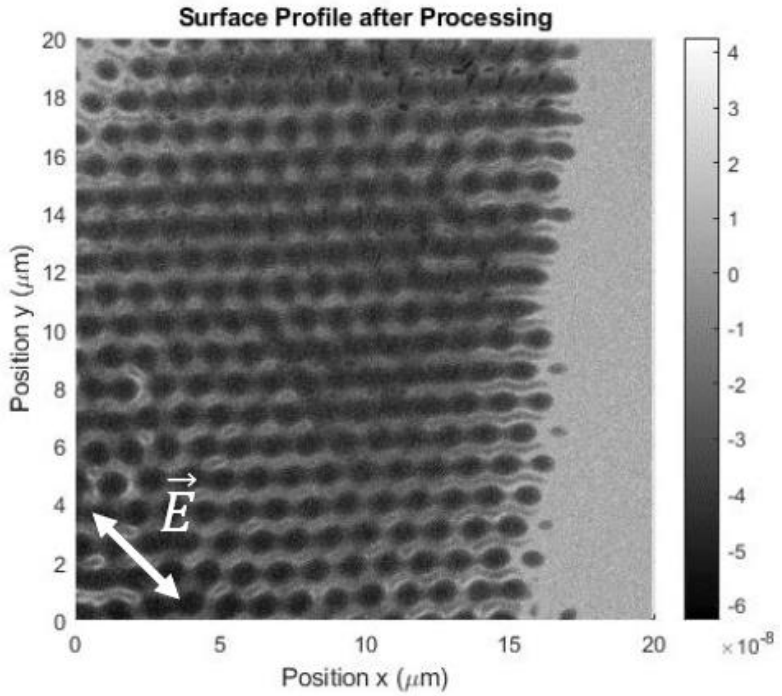

Figure 3.8. Simulation result of 45 degrees polarized light, $\vec{E}$ represents the polarization of incident laser light, scanning occurs in x direction, normal LIPSS, laser radius on the surface is 20 μm, scanning speed is 8 m/s, jump distance is 2 μm.

The surface scanning was carried out in the x direction, and the profile formed on the surface took a hexagon-like appearance. The scanning speed of the surface is 8 m/s in the x direction, jump distance, is 2 μm. The polarization of light is 45 degrees. The spatial wavelength or the period of LIPSS is approximately 0.9 μm.

The surfaces obtained with the simulation software changed between parallel lines and hexagonal surface structures during the parameter scanning for different surface structuring types. The surface structuring mostly occurs in the form of lines as expected. For certain values of scanning speed and jump speed it is observed that we can obtain hexagonal shapes with linearly polarized laser with a single scan of the surface.

CHAPTER 4

THE EXPERIMENTAL SETUP AND FABRICATION

In this chapter, the properties of the experimental setup are shown and the fabricated structures in the scope of thesis study are introduced. The aim in this thesis was to obtain different surface structures specifically hexagonal structuring on the surfaces of bulk Ti samples. In order to fabricate these structures a LIPSS setup with a custom-built fiber laser system is utilized. This system is connected to a galvoscanner and 3D stage. In the first section of this chapter, the experimental setup is examined. The femtosecond laser setup and its properties will be given. Then, the galvo-scanner and the connected 3D stage are inspected. In the second section of this chapter, the preparation of the samples for the fabrication are examined. In the last section of this chapter, the process parameters and the fabricated structures are given.

4.1 Experimental Information

The experimental setup used in this study has two important parts, femtosecond laser and galvoscanner stage. The femtosecond laser in our lab is a custom-built passive mode-locked laser that has 1 MHz repetition rate with a pulse duration 300 fs (which is shown in Figure 4.1.a, the autocorrelation measurement result shows FWHM of 428 fs). Its pulse energy can go up to 2 μJ. Its output spectrum is centered around 1030 nm. Autocorrelation measurement result for the pulse width, and spectrum of the laser is shown in Figure 4.1. The laser spot size at the focal point is approximately 20 μm.

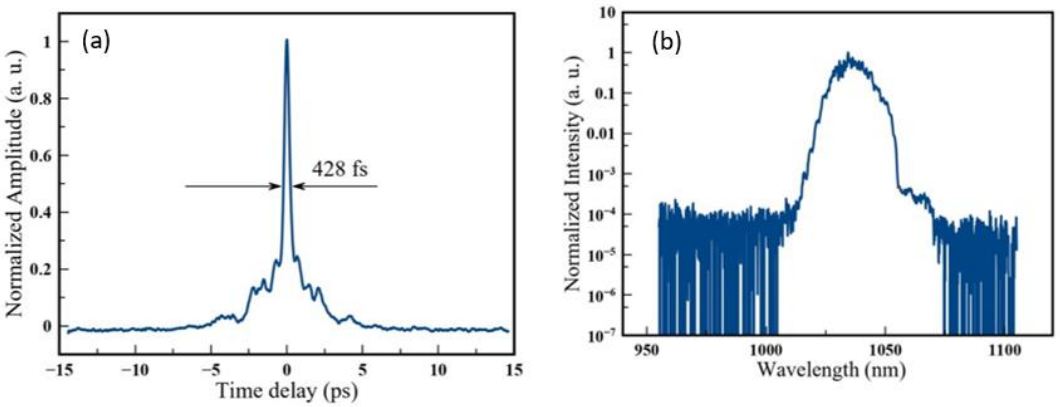

Figure 4.1. (a) Autocorrelation measurement result for time domain signal from femtosecond laser setup, (b) output spectrum of the laser.

The pulses move through a half-wave plate (HWP) and a polarization beam splitter (PBS). The intensity of the laser is modified using these two components. After going through them, the laser goes through another half-wave plate which controls the angle between the polarization of laser light and scanning direction. The sketch of custom-built LIPSS setup is shown in Figure 4.2. In Figure 4.3, the beam delivery path and in Figure 4.4 image of the setup is shown.

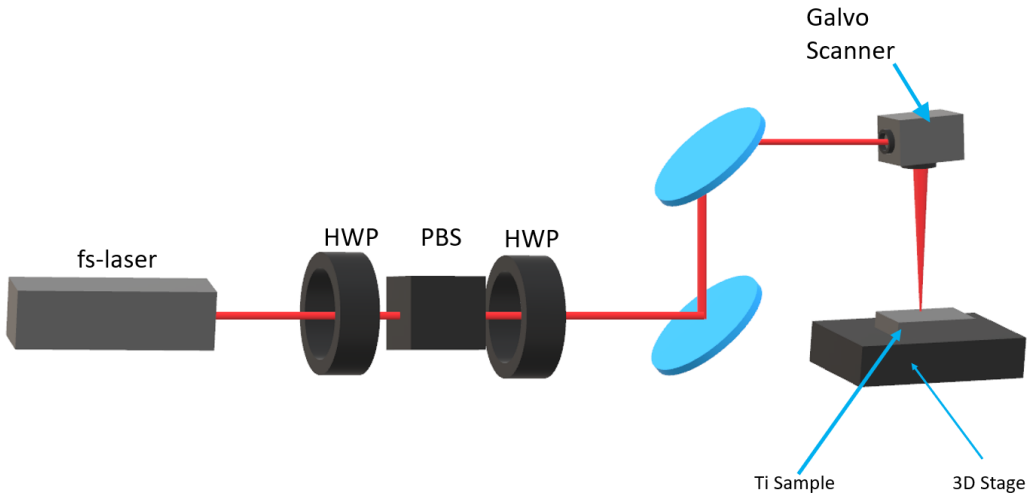

Figure 4.2. Sketch of custom-built LIPSS setup.

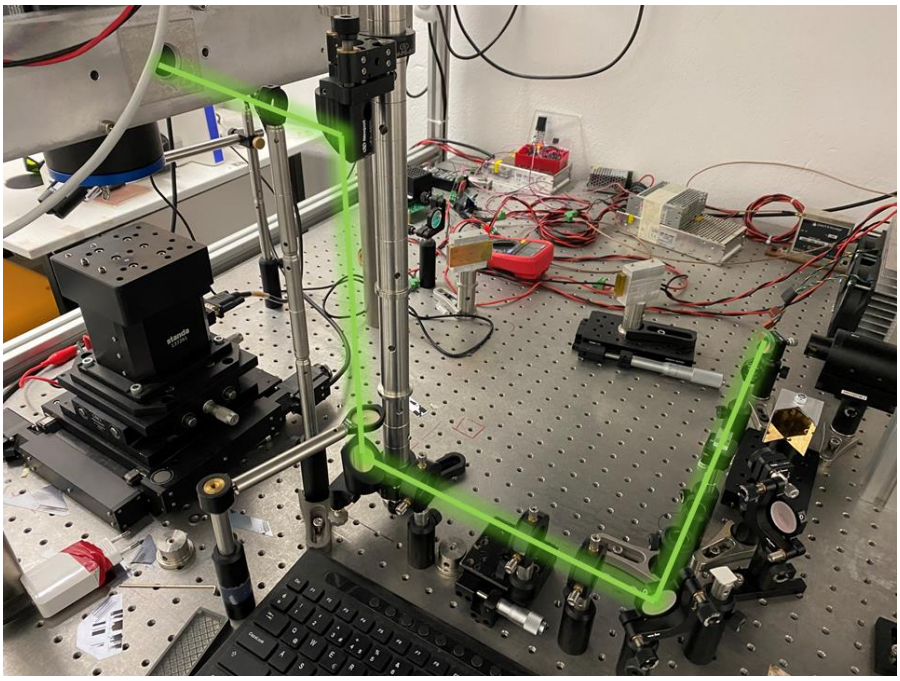

Figure 4.3. Beam delivery path.

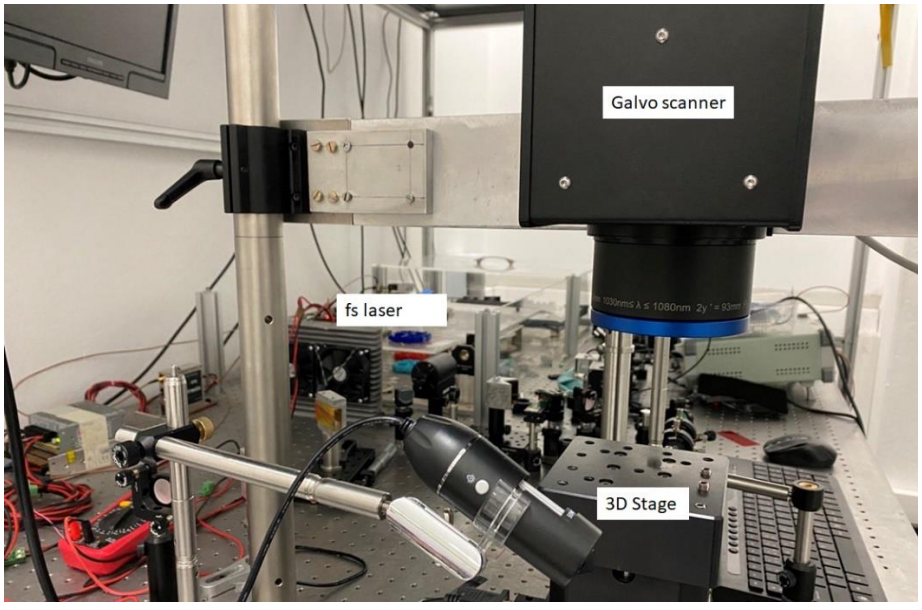

Figure 4.4. Image of LIPSS setup.

The Intelliscan III 14 is used as galvo-scanner in our setup. It has an aperture size of 14 mm and focal length of 100 mm. The scanning speed of the system is defined as 5 m/s in its datasheet, however the scanning speed can go up to 36 m/s.

4.2 Sample Preparation

The sample surfaces used in the LIPSS generation process are mirror polished bulk Ti discs and Ti coated Si wafers. Grade 2 Ti samples are used in the study to have nearly pure material (~99.3250%). Bulk Ti samples are bought as 30 cm rods and then cut in 5 mm pieces with wire cutting. Then, they are polished with sandpaper. The polishing process started with 240 grain sandpaper and ended with 10000 grain sandpaper. After that, in order to obtain mirror-like surface, it is polished with a finalizing paste. The images of the samples before and after the polishing is shown in Figure 4.5. In addition to the bulk titanium samples, there is a titanium coated silicon wafer sample. The sample is first cleaned with piranha solution to get rid of organic materials on the surface. Then, it is coated with Ti.

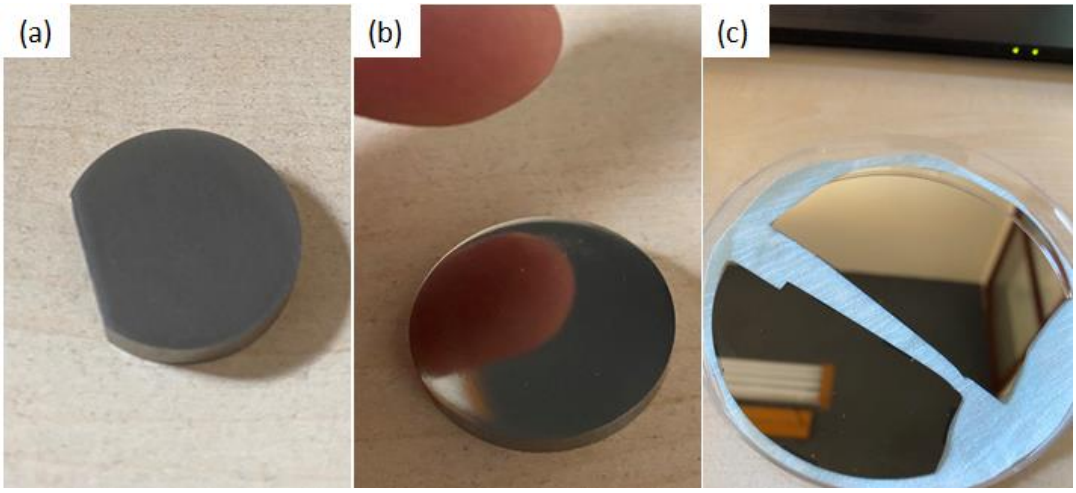

Figure 4.5. The samples (a) before and (b) after the polishing process, (c) titanium coated on Si.

4.3 Fabricated LIPSS

In order to obtain the structuring that this study aimed, several LIPSS are fabricated. Examples of fabricated normal LIPSS and their 2D Fourier Transforms are shown in Figure 4.6, Figure 4.7. The spatial wavelength of the structures is compatible with the theoretical calculations.

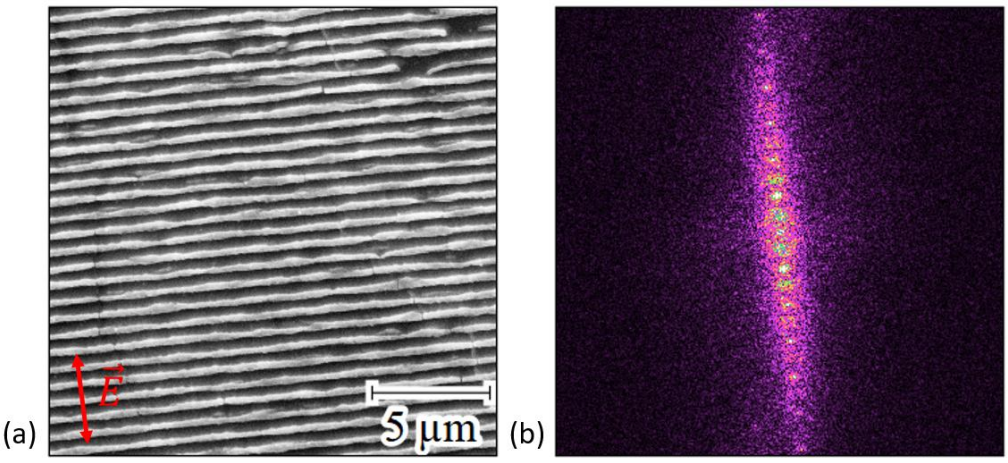

Figure 4.6. (a) Normal LIPSS, Power: 0.84W, Scan Speed: 5 m/s, Jump Speed: 5m/s, 50 Pulse per Focal Area, $\Lambda = 0.9\mu m$, red arrow shows the polarization of incident electric field, (b) 2D Fourier Transform of the structures in (a).

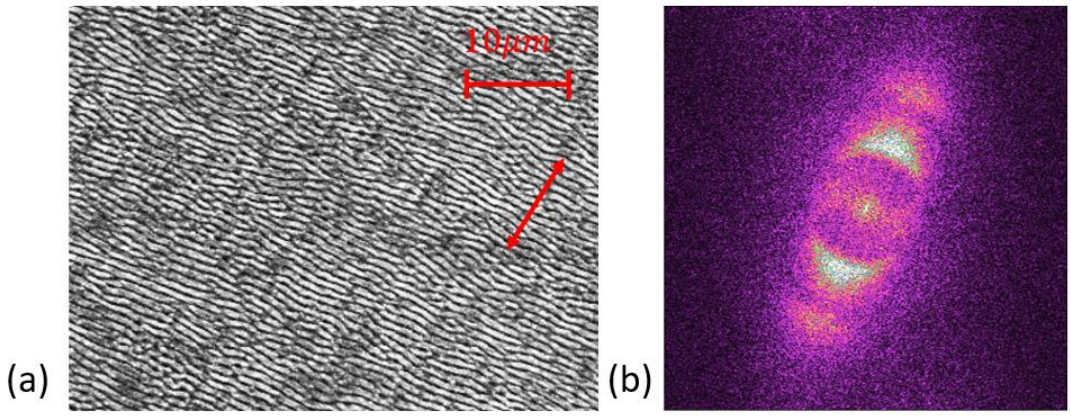

Figure 4.7. (a) Normal LIPSS, Power = 1.292W, Scan Speed 8m/s, Jump Speed = 7m/s, 22 Pulse Per Focal Area, $\Lambda = 0.9\mu m$, red arrow shows the polarization of incident electric field, (b) 2D Fourier Transform of LIPSS formation in (a).

4.3.1 Hexagonal LIPSS

One part of our experimental studies was creation of the hexagonal structure predicted experimentally and described in previous chapter. The structuring should be obtained in one run with linear polarization. The surface that hexagonal structuring occurred is shown in Figure 4.8.

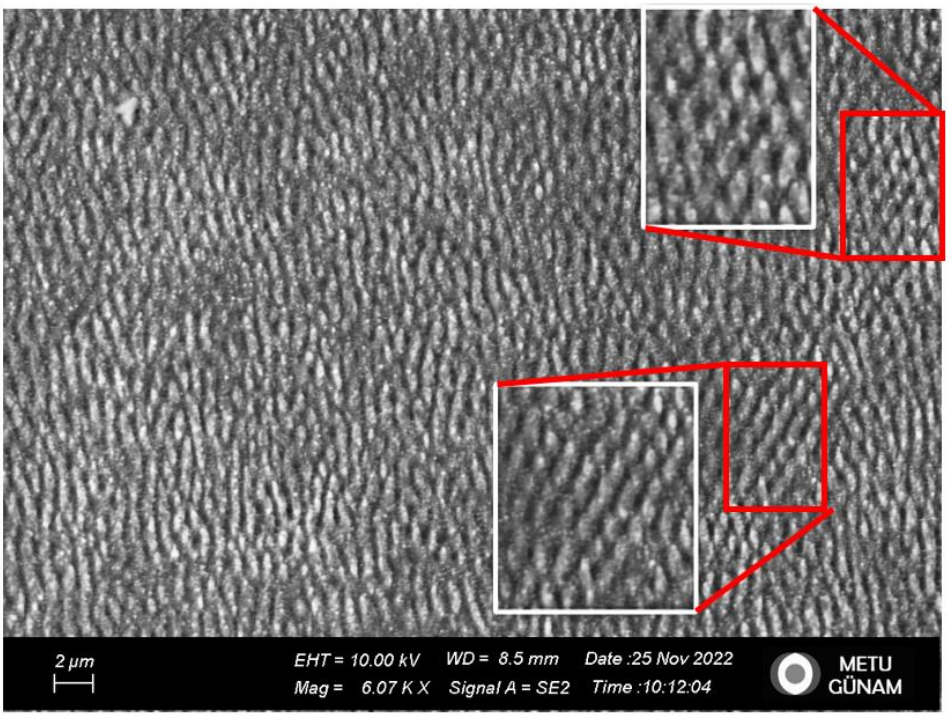

Figure 4.8. Example of hexagonal structure produced on Ti surface, laser radius on the surface is 20 µm, polarization is 45°, scanning speed is 8 m/s, jump distance is 2 µm.

Structuring on the surface of Ti happened on certain regions. The sample surface suffered from long-range uniformity. This is thought to be due to the poor surface quality.

4.3.2 Comparison of Fabricated and Simulated Hexagonal LIPSS

The simulated and fabricated structures are shown in Figure 4.9, Figure 4.10. The hexagonal structuring on the surface of Ti and the simulation result have similar periods.

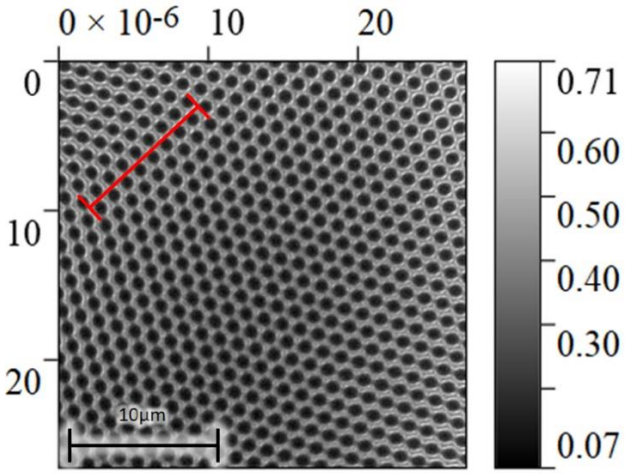

Figure 4.9. The simulated structure with distances shown on it, the average radius of 1 hole is approximately 0.9 μm, the period of holes is around 1.25 μm.

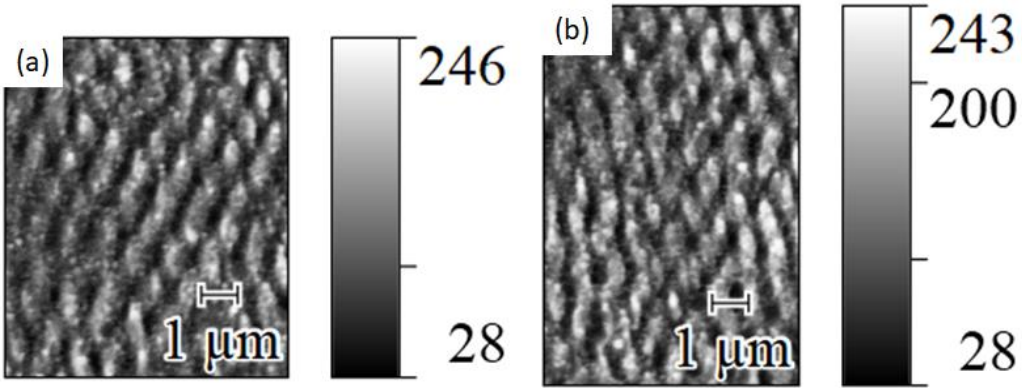

Figure 4.10. The fabricated structure with distances shown on it, the hole radius is approximately 0.5 μm, the period of hole is around 1.22 μm.

CHAPTER 5

CONCLUSION

In this thesis study, a simulator for laser-induced periodic surface structuring (LIPSS) is created and the structure formation was investigated for different laser parameters such as laser intensity, scan speed, jump distance and polarization. The theoretical model is created using surface scattered electromagnetic wave approach. The model is used to create a simulation software for LIPSS. The simulated structures are fabricated on Ti surfaces.

The electromagnetic interaction and surface thermochemical reactions are modelled and integrated into the simulation software. The model used for the electromagnetic interaction is based on light scattering from a nanoparticle [3, 13,19,20]. Since on the surface of a mirror-like polished sample where the average dimension of a nonuniformity is much smaller than the wavelength of the light, scattering from a nanoparticle approximation suited the electromagnetic interaction. Surface profile modification part mainly focused on the material removal from the surface. To model the material removal from the surface, a threshold intensity is calculated [21,22]. This threshold intensity is calculated as the summation of heating, melting and vaporization energies. The surface scanning parameters are inspected for different types of surface structures.

Ablation type LIPSS simulations are carried out on the simulation software. Simulator is first used for simple structures such as normal LIPSS with lines perpendicular to the polarization of the incident laser light. The validity of the software and theoretical model is proved by the simulation results for periodic lines. In addition to that, the surface scanning parameters and laser energy to obtain different types of structures by single scan with linearly polarized light (particularly hexagonal surface structures) are found with the help of simulation software. It is

observed that it is possible to obtain hexagonal surface structures with linearly polarized light by a single scan on the surface.

On the other hand, in the fabrication part of this study faced some challenges in terms of long-range uniformity of the fabricated structures. This study was able to successfully demonstrate the feasibility of fabricating hexagonal LIPSS.

In terms of future work, the study has opened up several options for further research in normal LIPSS fabrication and simulation. In addition to the studies that are possible with Ti samples, the use of different laser parameters and materials is possible in order to improve the long-range uniformity of the fabricated structures. Additionally, the simulation model developed in this study can be used to predict the formation of LIPSS patterns under different laser conditions and materials, which can be used to guide the fabrication of LIPSS structures for specific applications.

For the first time to the best of our knowledge, we demonstrated both theoretically and experimentally the formation of hexagonal LIPSS on Ti surface by a single scan with linearly polarized light. In addition, several other new types of structure are predicted. We believe the findings have created several avenues for more study in this area and has the potential to make significant contributions to disciplines including biology, optics, and electronics.

REFERENCES

[1] M. Birnbaum, ‘Semiconductor surface damage produced by Ruby lasers’, *Journal of Applied Physics*, vol. 36, pp. 3688–3689, 1965.

[2] Phillips, H.M., Callahan, D.L., Sauerbrey, R. et al. Direct laser ablation of sub-100 nm line structures into polyimide. *Appl. Phys*. A 54, 158–165 (1992).

[3] Jackson, J. (1975). *Classical electrodynamics. 2.Ed*. Wiley.

[4] Heitz, J., Arenholz, E., Bäuerle, D. et al. Femtosecond excimer-laser-induced structure formation on polymers. *Appl. Phys*. A 59, 289–293 (1994).

[5] Y. F. Lu, W. K. Choi, Y. Aoyagi, A. Kinomura, and K. Fujii, ‘Controllable laser-induced periodic structures at silicon-dioxide/silicon interface by excimer laser irradiation’, *Journal of Applied Physics*, vol. 80, pp. 7052–7056, 12 1996.

[6] J. Bonse, J. Krüger, S. Höhm, and A. Rosenfeld, ‘Femtosecond laser-induced periodic surface structures’, *Journal of Laser Applications*, vol. 24, p. 042006, 9 2012.

[7] T. Jwad, S. Deng, H. Butt, and S. Dimov, ‘Laser induced single spot oxidation of titanium’, Applied Surface Science, vol. 387, pp. 617–624, 11 2016.

[8] J. Bonse, S. Hohm, S. V. Kirner, A. Rosenfeld, and J. Kruger, ‘Laser-Induced Periodic Surface Structures-A Scientific Evergreen’, *IEEE Journal of Selected Topics in Quantum Electronics*, vol. 23, pp. 109–123, 5 2017.

[9] I. Pavlov, O. Yavuz, G. Makey, O. Toke, and O. Ilday, ‘Switching between normal and anomalous Laser Induced Periodic Surface Structures’, 10 2017.

[10] A. V. Dostovalov, V. P. Korolkov, V. S. Terentyev, K. A. Okotrub, F. N. Dultsev, and S. A. Babin, ‘Study of the formation of thermochemical laser-induced periodic surface structures on Cr, Ti, Ni and NiCr films under femtosecond irradiation’, Quantum Electronics, vol. 47, pp. 631–637, 7 2017.

[11] S. Gräf, ‘Formation of laser-induced periodic surface structures on different materials: Fundamentals, properties and applications’, Advanced Optical Technologies, vol. 469, pp. 904–910, 3 2020.

[12] J. Bonse and S. Gräf, ‘Ten open questions about laser-induced periodic surface structures’, Nanomaterials, vol. 11, 12 2021.

[13] J. Bonse and S. Gräf, ‘Maxwell Meets Marangoni—A Review of Theories on Laser-Induced Periodic Surface Structures’, Laser & Photonics Reviews, vol. 14, no. 10, p. 2000215, 2020.

[14] Y. H. Liu, S. C. Yeh, and C. W. Cheng, ‘Two-dimensional periodic nanostructure fabricated on titanium by femtosecond green laser’, Nanomaterials, vol. 10, pp. 1–11, 9 2020.

[15] P. B. Johnson and R. W. Christy. Optical constants of transition metals: Ti, V, Cr, Mn, Fe, Co, Ni, and Pd, *Phys. Rev. B* 9, 5056-5070 (1974)

[16] D. C. Emmony, R. P. Howson, and L. J. Willis, ‘Laser mirror damage in germanium at 10.6 μm’, Applied Physics Letters, vol. 23, pp. 598–600, 1973.

[17] P. Mannion, J. Magee, E. Coyne, and G. M. O’connor, ‘Ablation thresholds in ultrafast laser micro-machining of common metals in air’, 2003.

[18] V. Kara and H. Kizil, ‘Titanium micromachining by femtosecond laser’, Optics and Lasers in Engineering, vol. 50, pp. 140–147, 2 2012.

[19] L. Novotny and B. Hecht, Principles of Nano-Optics, 2nd ed. Cambridge: Cambridge University Press, 2012.

[20] S. A. Maier, ‘Localized Surface Plasmons’, in Plasmonics: Fundamentals and Applications, New York, NY: Springer US, 2007, pp. 65–88.

[21] S. Nolte *et al.*, ‘Ablation of metals by ultrashort laser pulses’, 1997.

[22] E. G. Gamaly, A. V. Rode, B. Luther-Davies, and V. T. Tikhonchuk, ‘Ablation of solids by femtosecond lasers: Ablation mechanism and ablation thresholds for metals and dielectrics’, Physics of Plasmas, vol. 9, p. 949, 3 2002.

[23] M. Kerker, ‘CHAPTER 3 - Scattering by a Sphere’, in The Scattering of Light and Other Electromagnetic Radiation, vol. 16, M. Kerker, Ed. Academic Press, 1969, pp. 27–96.

[24] V. I. Emel’yanov, E. M. Zemskov, and V. N. Seminogov, ‘Theory of the formation of “normal” and “anomalous” gratings on the surfaces of absorbing condensed media exposed to laser radiation’, *Soviet Journal of Quantum Electronics*, vol. 14, no. 11, p. 1515, Nov. 1984.

[25] J. E. Sipe, J. F. Young, J. S. Preston, and H. M. van Driel, ‘Laser-induced periodic surface structure. I. Theory’, *Phys. Rev. B*, vol. 27, pp. 1141–1154, Jan. 1983.

[26] Keilmann and Y. H. Bai, “Periodic surface structures frozen into CO2laser-melted quartz,” *Appl. Phys. A*, vol. 29, pp. 9–18, 1982

[27] J. Z. P. Skolski, G. R. B. E. Römer, J. V. Obona, V. Ocelik, A. J. H. I. ’t Veld, and J. T. M. D. Hosson, ‘Laser-induced periodic surface structures: Fingerprints of light localization’, *Physical Review B - Condensed Matter and Materials Physics*, vol. 85, 2 2012.

[28] A. Lübcke, Z. Pápa, and M. Schnürer, ‘Monitoring of evolving laser induced periodic surface structures’, Applied Sciences (Switzerland), vol. 9. MDPI AG, 9 2019.

[30] B. Öktem et al., ‘Nonlinear laser lithography for indefinitely large-area nanostructuring with femtosecond pulses’, *Nature Photonics*, vol. 7. pp. 897–901, 11 2013.

[31] P. A. Temple and M. J. Soileau, ‘Polarization Charge Model for Laser-Induced Ripple Patterns in Dielectric Materials’, *IEEE Journal of Quantum Electronics*, vol. 17, pp. 2067–2072, 1981.

[32] H. M. van Driel, J. E. Sipe, and J. F. Young, ‘Laser-Induced Periodic Surface Structure on Solids: A Universal Phenomenon’, *Phys. Rev. Lett*., vol. 49, pp. 1955–1958, Dec. 1982.

APPENDICES

A. SIMULATION FLOW AND INPUT OUTPUT LIST OF FUNCTIONS

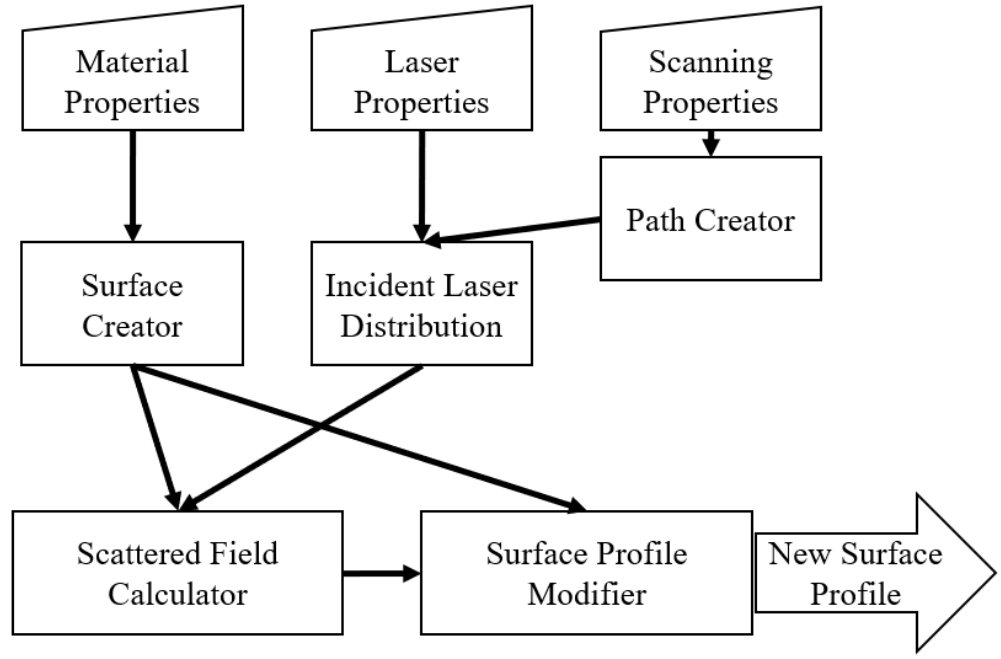

Figure A.1. Simulation Flow.

Table A-1. Input Output List of Sub Blocks.

Sub Block	Inputs	Outputs
Surface Creator	Space Limit, Space Step, Material Type	x coordinates, y coordinates, Surface Profile
Incident Laser Distribution Calculator	x coordinates, y coordinates, Maximum Intensity, Beam Width, Coordinates of the Center of the beam, Polarization Angle	Intensity Distribution
Path Creator	Scan Speed, Line Distance, Scan Direction	Coordinates of the center of the beam
Scattered Field Calculator	Intensity Distribution, Surface Profile	Intensity Distribution of the Interference
Surface Profile Modifier	Intensity Distribution of the Interference, Surface Profile	New Surface Profile